

# Tunable Electrical and Optical Characteristics in Monolayer Graphene and Few-Layer MoS<sub>2</sub> Heterostructure Devices

Servin Rathi,<sup>†</sup> Inyeal Lee,<sup>†</sup> Dongsuk Lim,<sup>‡</sup> Jianwei Wang,<sup>†</sup> Yuichi Ochiai,<sup>§</sup> Nobuyuki Aoki,<sup>§</sup> Kenji Watanabe,<sup>||</sup> Takashi Taniguchi,<sup>||</sup> Gwan-Hyoung Lee,<sup>⊥</sup> Young-Jun Yu,<sup>#</sup> Philip Kim,<sup>▽</sup> and Gil-Ho Kim<sup>\*,†</sup>

<sup>†</sup>School of Electronic and Electrical Engineering, and Sungkyunkwan Advanced Institute of Nanotechnology (SAINT) and <sup>‡</sup>School of Advanced Materials Science and Engineering, Sungkyunkwan University, Suwon 440-746, Korea

<sup>§</sup>Graduate School of Advanced Integration Science, Chiba University, 1-33 Yayoi-cho, Inage-ku, Chiba 263-8522, Japan

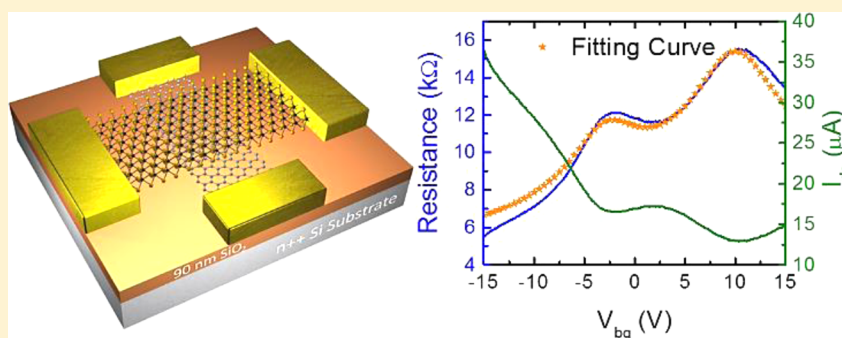
<sup>||</sup>Advanced Materials Laboratory, National Institute for Materials Science, 1-1 Namiki, Tsukuba, 305-0044, Japan

<sup>⊥</sup>Department of Material Science and Engineering, Yonsei University, Seoul 120-749, Korea

<sup>#</sup>Creative Research Center for Graphene Electronics and Telecommunications Research Institute (ETRI), Daejeon 305-700, Korea

<sup>▽</sup>Department of Physics, Harvard University, Cambridge, Massachusetts 02138, United States

## S Supporting Information



**ABSTRACT:** Lateral and vertical two-dimensional heterostructure devices, in particular graphene–MoS<sub>2</sub>, have attracted profound interest as they offer additional functionalities over normal two-dimensional devices. Here, we have carried out electrical and optical characterization of graphene–MoS<sub>2</sub> heterostructure. The few-layer MoS<sub>2</sub> devices with metal electrode at one end and monolayer graphene electrode at the other end show nonlinearity in drain current with drain voltage sweep due to asymmetrical Schottky barrier height at the contacts and can be modulated with an external gate field. The doping effect of MoS<sub>2</sub> on graphene was observed as double Dirac points in the transfer characteristics of the graphene field-effect transistor (FET) with a few-layer MoS<sub>2</sub> overlapping the middle part of the channel, whereas the underlapping of graphene have negligible effect on MoS<sub>2</sub> FET characteristics, which showed typical n-type behavior. The heterostructure also exhibits a strongest optical response for 520 nm wavelength, which decreases with higher wavelengths. Another distinct feature observed in the heterostructure is the peak in the photocurrent around zero gate voltage. This peak is distinguished from conventional MoS<sub>2</sub> FETs, which show a continuous increase in photocurrent with back-gate voltage. These results offer significant insight and further enhance the understanding of the graphene–MoS<sub>2</sub> heterostructure.

**KEYWORDS:** 2D semiconductor, graphene, molybdenum disulfide, heterostructure, Schottky barrier, field-effect transistor

The van der Waals heterostructures consisting of various two-dimensional (2D) materials, such as graphene, transition metal dichalcogenides of molybdenum disulfide (MoS<sub>2</sub>), and tungsten diselenide (WSe<sub>2</sub>), and insulating dielectrics of hexagonal-boron nitride (h-BN) have given rise to many interesting results and phenomena that have not only enriched the physical understanding of 2D systems but have also broadened the scope for their applications.<sup>1–10</sup> It has been demonstrated that such van der Waals heterostructures can be used for novel 2D devices, such as vertical transistors, resonant tunneling diodes, photodetectors, and photoresponsive mem-

ory.<sup>2,4,11–13</sup> Of these heterostructures, the combination of graphene and MoS<sub>2</sub> is especially interesting because of various factors including the excellent optical properties of MoS<sub>2</sub>, tunability of graphene's Fermi level, and high transparency of graphene. The consequences and applications of these properties in graphene–MoS<sub>2</sub> heterostructure have been

**Received:** March 15, 2015

**Revised:** May 26, 2015

**Published:** June 19, 2015

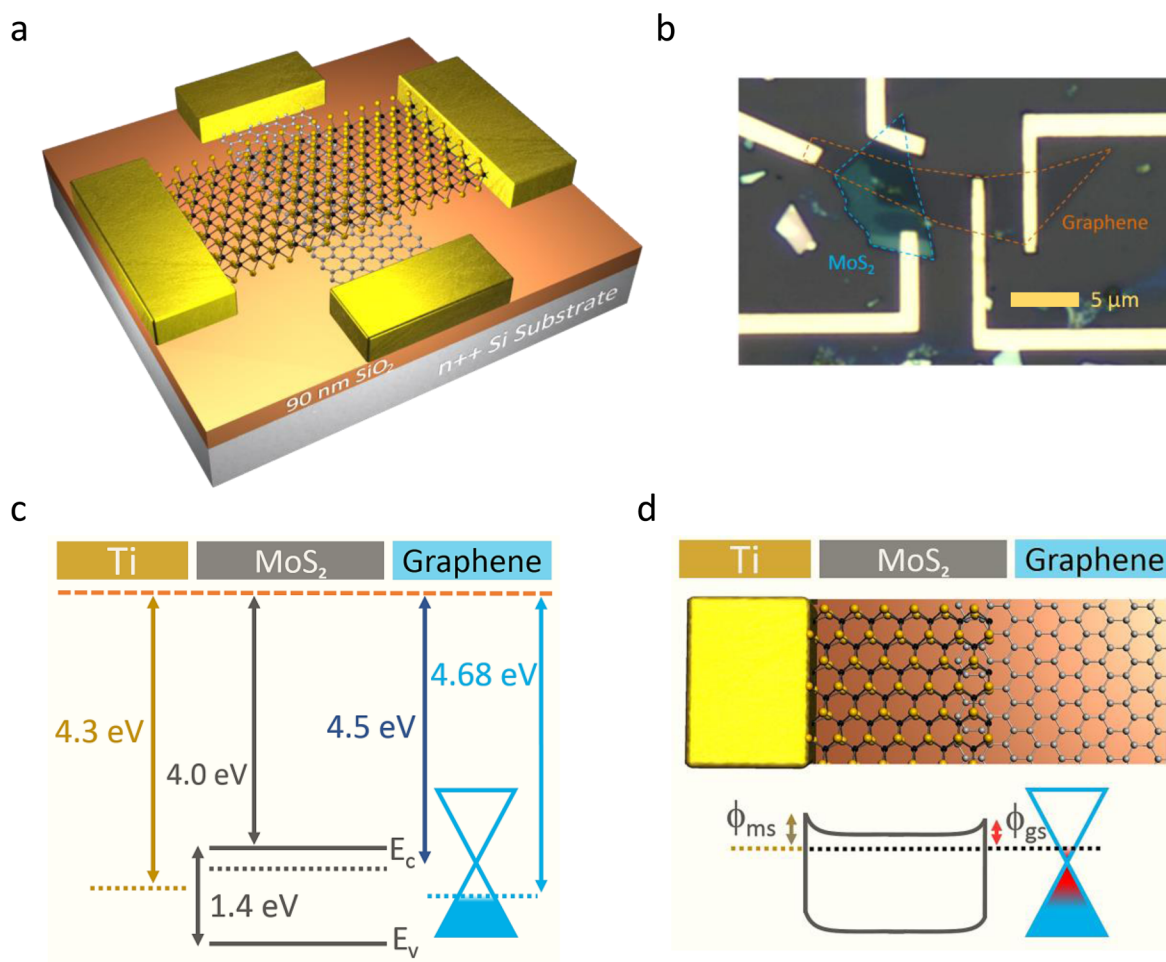


**Figure 1.** (a) Schematic and (b) microscopic images of the graphene–MoS<sub>2</sub> heterostructure device. Energy band diagrams of the proposed device geometry with Ti metal and graphene contact in the (c) isolated and (d) connected state. On the basis of work function difference, asymmetric Schottky barriers are formed at metal and graphene contacts to MoS<sub>2</sub>. For metal–MoS<sub>2</sub>, the barrier height is fixed while for graphene–MoS<sub>2</sub> junction, it depends on the doping level in graphene.

studied in this work through electrical and optical measurements. Similar to the barrier formation at the metal–MoS<sub>2</sub> contact, the heterointerface of MoS<sub>2</sub> and graphene also leads to the formation of Schottky barrier due to the difference in work function, which is supported by the observation of double Dirac points in the heterostructure devices. The different work functions of metal and graphene contact make asymmetric barriers to the MoS<sub>2</sub> layer, which results in rectifying current–voltage characteristics. As graphene forms a lower barrier with MoS<sub>2</sub> than typical Ti/Au contact, it results in better electrical performance of MoS<sub>2</sub> field-effect transistors (FETs).<sup>14–16</sup> Further, 2D-based devices also exhibit pronounced response to the optical signals, which can be modulated with an applied electric field.<sup>17–20</sup> Thoughh, earlier work focused mainly on vertical current flow in the heterostructures,<sup>1,2</sup> whereas the asymmetrical contacts of MoS<sub>2</sub> with metal on one and graphene on the other end are systematically studied in this work. Optical response measurement from the global illumination with various wavelength shows unique light–matter interaction in MoS<sub>2</sub>–graphene heterojunction, such as peak photocurrent and gate-tunability.

For the device fabrication, graphene and MoS<sub>2</sub> were mechanically exfoliated using the scotch tape method. The graphene was exfoliated directly on a 90 nm SiO<sub>2</sub>/Si wafer, followed by a transfer of exfoliated MoS<sub>2</sub> using typical transfer

technique (for details, see Supporting Information, Section A). The connecting electrodes were fabricated by using e-beam lithography and metal deposition of Ti/Au (10 nm/100 nm). Figure 1a,b shows the schematic and microscopic image of the fabricated device, respectively. The thickness of graphene and MoS<sub>2</sub> were investigated by Raman spectroscopy and found out to be a single and a few-layers, respectively (for details, see Supporting Information, Section B). The band diagrams of the constituent layers in the isolated and connected state are shown in Figure 1c,d, respectively. In general, MoS<sub>2</sub> display n-type behavior due to sulfur vacancies and other lattice impurities,<sup>21,22</sup> and the energy band gap ( $E_g$ ) and electron affinity ( $\chi_{\text{MoS}_2}$ ) of few-layer MoS<sub>2</sub> are  $\approx 1.4$  and 4.0 eV, respectively.<sup>23,24</sup> For pristine monolayer graphene, the work function ( $\phi_g$ ) at the Dirac point is taken to be 4.5 eV,<sup>6,7</sup> but graphene in our work is highly p-doped, as found from electrical measurements, probably due to charged impurities in the underlying substrate, adsorbates, and polymer residue.<sup>25</sup> The Fermi energy level of p-doped graphene is calculated from the shift in the charge neutral point in the electrical characteristics and found to be  $\approx 0.18$  eV below the Dirac point, which corresponds to a work function of 4.68 eV (for details, see Supporting Information, Section C) Therefore, as seen in Figure 1d, the work-function difference of MoS<sub>2</sub> with metal and graphene results in

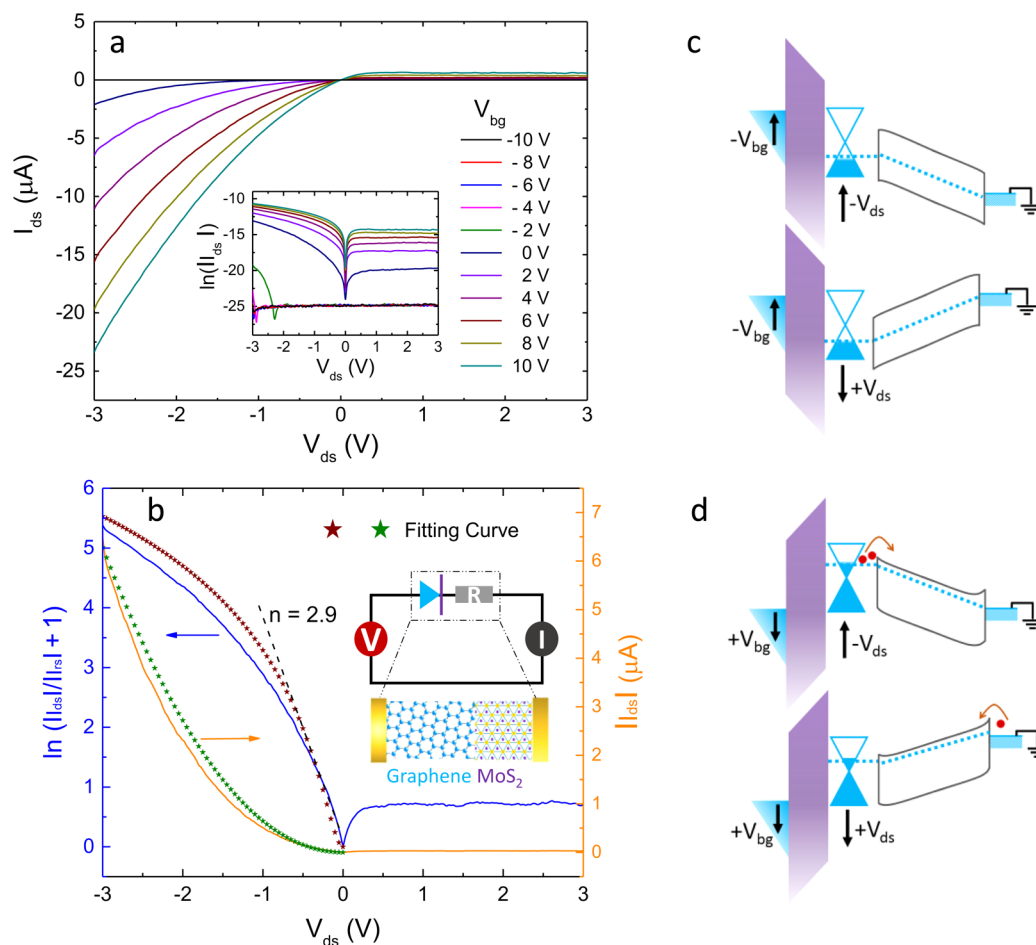


**Figure 2.** Electrical characteristics of the MoS<sub>2</sub>–graphene heterostructure device. (a) Current versus drain voltage curve at various back-gate voltages for grounded MoS<sub>2</sub>; the inset shows the semilog curves. (b) Measured and fitted curve at the back-gate voltage of +2 V; the inset shows the schematic of the measured device. (c,d) Energy band diagrams showing band alignments at negative and positive back-gate voltages, respectively.

asymmetric barrier formation at these junctions. As graphene has low density of states (DOS) near its Dirac point, its work function can be easily modulated by an external electric field.<sup>15</sup> Thus, the variable barrier height at graphene–MoS<sub>2</sub> heterojunction can be employed for additional functionalities in such devices.

Electrical characterization of the device was then performed for both symmetrical and asymmetrical contacts. The symmetrical contacts refer to the case where metal contacts are used for both source and drain, whereas, when one side is connected by metal and the other by graphene, such configuration is referred as asymmetrical contacts. As seen in Figure 1b, the fabricated device can be measured in both asymmetrical and symmetrical contact modes. First, the asymmetrical combination with metal and graphene contacts to MoS<sub>2</sub> (left graphene– and top metal–MoS<sub>2</sub> contacts in Figure 1b) was measured as shown in Figure 2a, where rectifying curves, well-modulated by the applied back-gate voltage ( $V_{bg}$ ), are obtained. (for other asymmetrical contact in Figure 1b, see Supporting Information, Section D) The observed rectifying behavior can be explained by the asymmetric Schottky barrier formation between the metal–MoS<sub>2</sub> and graphene–MoS<sub>2</sub> contacts.

As seen in Figure 2a, on-current in the negative drain bias can be modulated by the back-gate voltage, that is, for the positive back-gate voltage, the on-current increases, and vice

versa. However, the off-current in the positive drain side shows a weaker dependence on the back-gate voltage. This is because unlike in metals, the Fermi level of graphene can be modulated by the applied gate voltage, that is, vertical electric field can modulate the graphene Fermi level because of the low density of states (DOS) in graphene.<sup>12</sup> This gate-modulation of graphene's Fermi level results in the variation of barrier height ( $\phi_{gs}$ ) at the graphene–MoS<sub>2</sub> contact, whereas the barrier height ( $\phi_{ms}$ ) at the metal–MoS<sub>2</sub> contact remains relatively constant.<sup>26</sup> This has also been illustrated schematically in Figure 2c,d for negative and positive back-gate voltages, respectively. For positive gate voltage ( $+V_{bg}$ ), the Fermi level of graphene shifted upward which decreases its work function, thus reducing the barrier height,  $\phi_{gs}$  ( $= \phi_g - \chi_{\text{MoS}_2}$ ). This reduction in the barrier height along with a higher electron concentration in MoS<sub>2</sub> leads to an increase current in the negative drain bias region, whereas for positive drain bias ( $+V_{ds}$ ), the dominating barrier is the metal–MoS<sub>2</sub> junction that, being higher than the graphene–MoS<sub>2</sub> barrier, results in the lower current. Furthermore, the current at this junction that shows weaker dependence on the back-gate voltage, increases marginally with contribution from tunneling and thermionic field emissions for positive back-gate voltage.

In contrast, the negative back-gate voltage not only leads to an increase in  $\phi_{gs}$  due to hole doping in the graphene but also reduces the electron concentration in MoS<sub>2</sub>, which results in

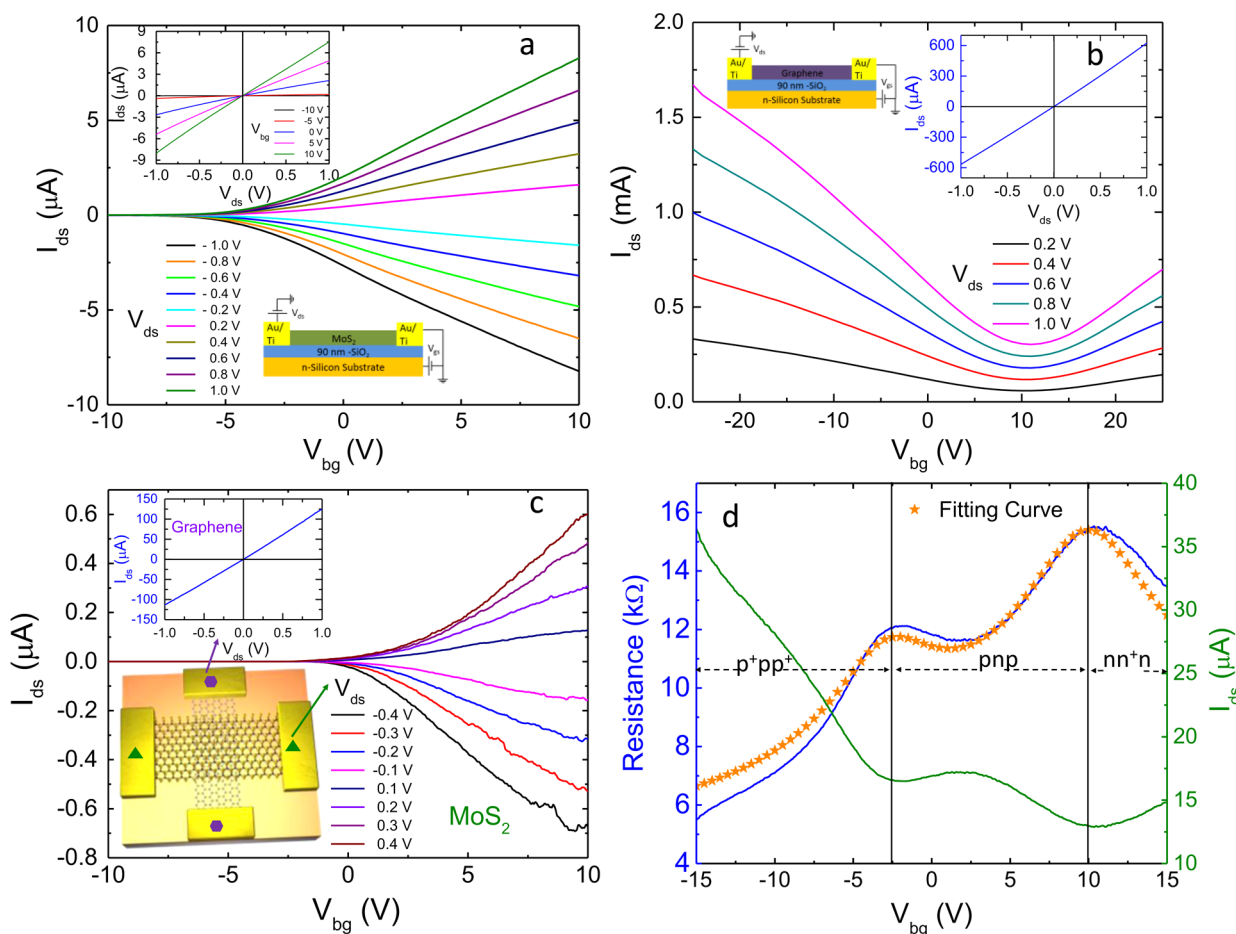


**Figure 3.** (a) Transfer characteristics of the few-layer MoS<sub>2</sub> transistor on SiO<sub>2</sub> with the inset showing linear curves for good ohmic contacts. (b) Transfer characteristics of the graphene FET showing typical p-type behavior with the inset displaying a linear ohmic behavior. (c) Transfer characteristics of the hybrid heterostructure with both metal contacts connected to MoS<sub>2</sub>. The upper inset shows good ohmic behavior of the graphene layer, while the device schematic in the lower inset highlights the measured contacts. (d) Resistance variation and transfer characteristics showing double Dirac point, with star symbols indicate the fitting curve using eq 2.

lower current for both negative and positive drain voltages. Finally, the device turned off when the back-gate voltage crossed the threshold voltage of the MoS<sub>2</sub> layer, where electrons are fully depleted in the channel (for details, see Supporting Information, Section E). The rectifying curves in Figure 2a,b, resemble typical semiconductor diode behavior and were analyzed using typical diode equations. The ideality factor,  $n$ , can be derived from the slope of the  $\ln(|I_{ds}|/|I_{rs}| + 1)$  versus  $V_{ds}$  curve from Figure 2b (for details, see Supporting Information, Section F). Such a gate-tunable diode behavior can be used for tunable rectification of an alternating signal. (for details, see Supporting Information, Section G)

With the electrical characterization of the asymmetrical contacts to MoS<sub>2</sub>, the symmetrical metal contacts to both graphene and MoS<sub>2</sub> are studied as follows. Figure 3 plots the curves for symmetrical contacts, where Figure 3a,b plots the results from other similar devices fabricated along with the device in Figure 1b, while the curves in Figure 3c,d were obtained from the device shown in Figure 1b. As observed in Figure 3a,b, well-defined transfer characteristics were obtained for both few-layer MoS<sub>2</sub> and bilayer graphene devices. As expected, MoS<sub>2</sub> device exhibits n-type behavior with a threshold voltage of around  $-8$  V, whereas the graphene device exhibits ambipolar behavior with a shift in Dirac point to  $+10$  V due to hole doping by substrate impurities and other polymer residues.

The insets of Figure 3a,b show linear output curves, illustrating Ohmic contact formation in both MoS<sub>2</sub> and graphene devices. In addition to other device parameters, the field-effect mobility ( $\mu_{FE}$ ) can be obtained from the transfer characteristics using the following expression

$$\mu_{FE} = \frac{L}{WC_{ox}} \frac{dI_{ds}}{V_{ds} dV_{bg}} \quad (1)$$

where  $C_{ox}$  is the oxide capacitance per unit area given by  $(\epsilon_0 \epsilon_r)/d$  ( $\epsilon_0$  is the absolute permittivity and  $\epsilon_r$  is the dielectric constant of SiO<sub>2</sub> of thickness  $d$ ),  $L$  and  $W$  are the device channel length and width, respectively,  $V_{ds}$  is the applied drain bias, and  $dI_{ds}/dV_{bg}$  is the transconductance. For 90 nm thick SiO<sub>2</sub>,  $C_{ox}$  is 38.3 nF cm<sup>-2</sup> and the field-effect mobility values at room temperature are calculated to be  $\sim 55$  and 500 cm<sup>2</sup> (Vs)<sup>-1</sup> for few-layer MoS<sub>2</sub> and bilayer graphene, respectively. The obtained values are in agreement with mobilities reported by others.<sup>18,22,27,28</sup> Furthermore, the field effect mobility of  $\sim 15$  cm<sup>2</sup> (Vs)<sup>-1</sup> is obtained from the transfer characteristics of the symmetrically metal connected MoS<sub>2</sub> (Figure 3c); this decrease in mobility can be due to the additional barrier formation from charge transfer to the underlapped graphene or polymer residues. In Figure 3, panels c (inset) and d, the symmetrical metal-contacted graphene layer was characterized by linear



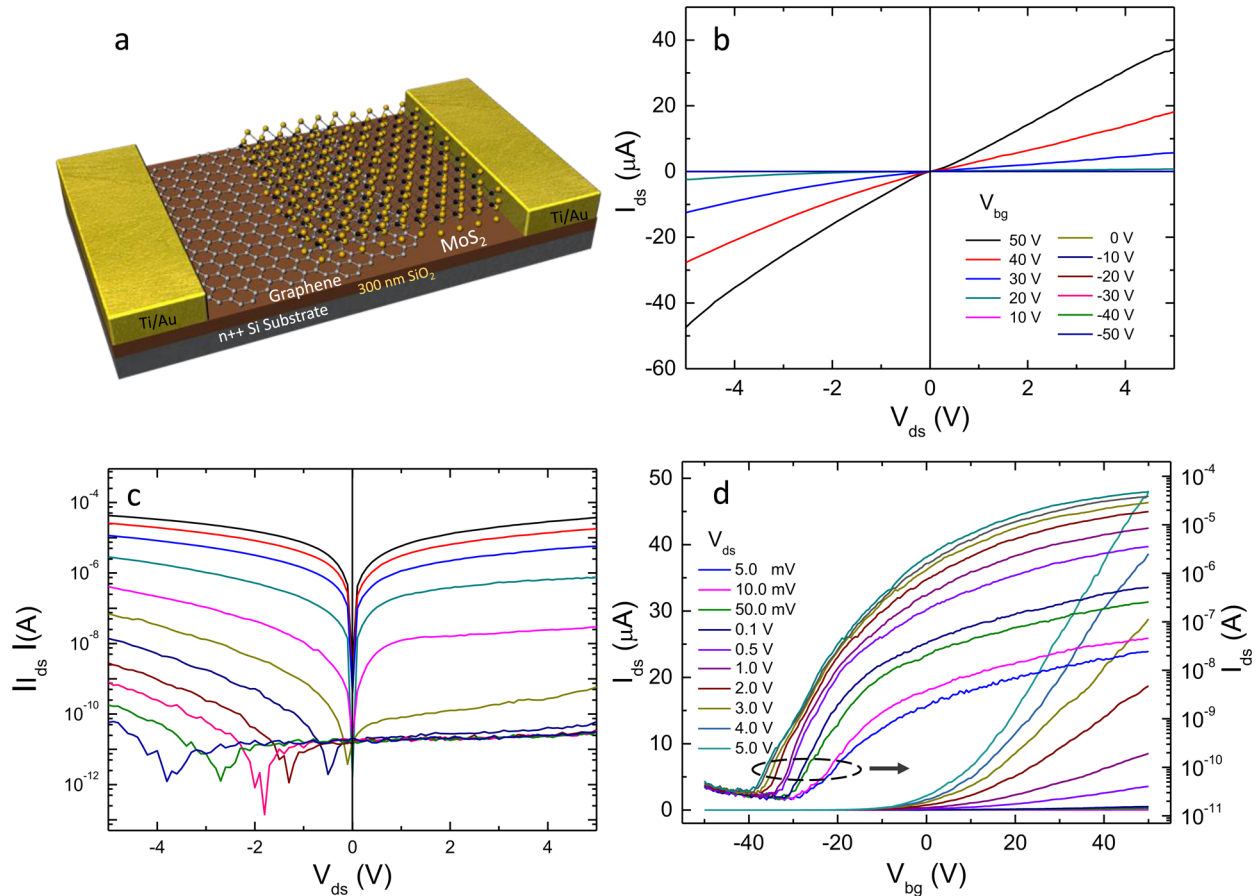


**Figure 4.** (a) Schematic of graphene–MoS<sub>2</sub> hybrid device on a 300 nm SiO<sub>2</sub> substrate. (b) Current versus drain bias curve for back-gate voltage varying from –50 to 50 V with (c) showing the semilog plots. (d) Transfer characteristics of the hybrid device for drain voltage varying from 5.0 mV to 5 V with current plotted in the log scale on the secondary axis.

output curve and double-Dirac transfer curve, respectively. One possible reason for the observation of the double-Dirac curve could be the additional doping from the MoS<sub>2</sub> layer in the overlapped region. However, various other causes have been analyzed before reaching to any conclusion; one cause for the observation of double-Dirac points is the unpinning of the Fermi level under the metal contacts, possibly due to the formation of thin oxide layers or intermittent residues, which leads to the formation of a p–n junction at low drain bias.<sup>29</sup> However, this explanation is not valid in our case because several graphene devices, which were fabricated with both Ti/Au and Cr/Au contacts, showed well-defined single Dirac curves with a p-type behavior. Another instance for such an observation in graphene is high negative gate stress with high-drain-bias-induced lateral p-type doping, which was also not observed in the device.<sup>30</sup> In addition to the above factors, multiple Dirac points can be observed in graphene either due to local gates or chemical-doping-induced p–n junction formation. Therefore, in Figure 3d, the double-Dirac points are possibly due to the charge transfer from the MoS<sub>2</sub> to graphene, which results in an additional doping in the graphene. This charge transfer and the observation of the double-Dirac points have also been modeled using the following equation<sup>31–33</sup>

$$R_T = R_C + \frac{1}{q\mu_1} \left( \frac{L_1}{W_1} \right) \frac{1}{\sqrt{n_{01}^2 + n_1^2}} + \frac{1}{q\mu_2} \left( \frac{L_2}{W_2} \right) \frac{1}{\sqrt{n_{02}^2 + n_2^2}} \quad (2)$$

where  $R_C$  is the contact resistance and  $\mu_1$  ( $\mu_2$ ),  $L_1$  ( $L_2$ ),  $W_1$  ( $W_2$ ),  $n_{01}$  ( $n_{02}$ ), and  $n_1$  ( $n_2$ ) are the mobility, length, width, residual carrier, and back-gate modulated carrier density in the device nonoverlap (overlap) region, respectively. In general, the expression for the back-gate modulated carrier concentration can be expressed as  $n = C_{ox}(V_{bg} - V_{bg0})/q$ , where  $V_{bg0}$  and  $q$  are the Dirac point and the electron charge, respectively. Although, the transfer charge may have a back-gate dependence but for simplicity, it was considered as a constant quantity. Using the known values, the double-Dirac curve was fitted with eq 2 and the best fit was obtained for  $\mu_1$  ( $\mu_2$ )  $\approx$  477 (980) cm<sup>2</sup> (V·s)<sup>–1</sup> with the transferred charge of  $\sim 3.2 \times 10^{12}$  cm<sup>–2</sup>. This can also be verified from the difference in the Dirac point voltages ( $\Delta V$ ), that is,  $n_{tr} = (C_{ox}\Delta V)/q = 2.99 \times 10^{12}$  cm<sup>–2</sup> for 12.5 V, which is consistent with the fitted value. Therefore, the region marked as p<sup>+</sup>pp<sup>+</sup>, pnp and nn<sup>+</sup>n in Figure 3d can be explained as follows: for far negative back-gate voltage, the nonoverlap regions are more heavily hole-doped (p-type) as compared to the overlapped region, so as voltage is swept to the right the lightly doped region reaches the neutral point first as compared to the nonoverlapped regions which results in the observation of first Dirac peak (–2.5 V), beyond this point the overlap

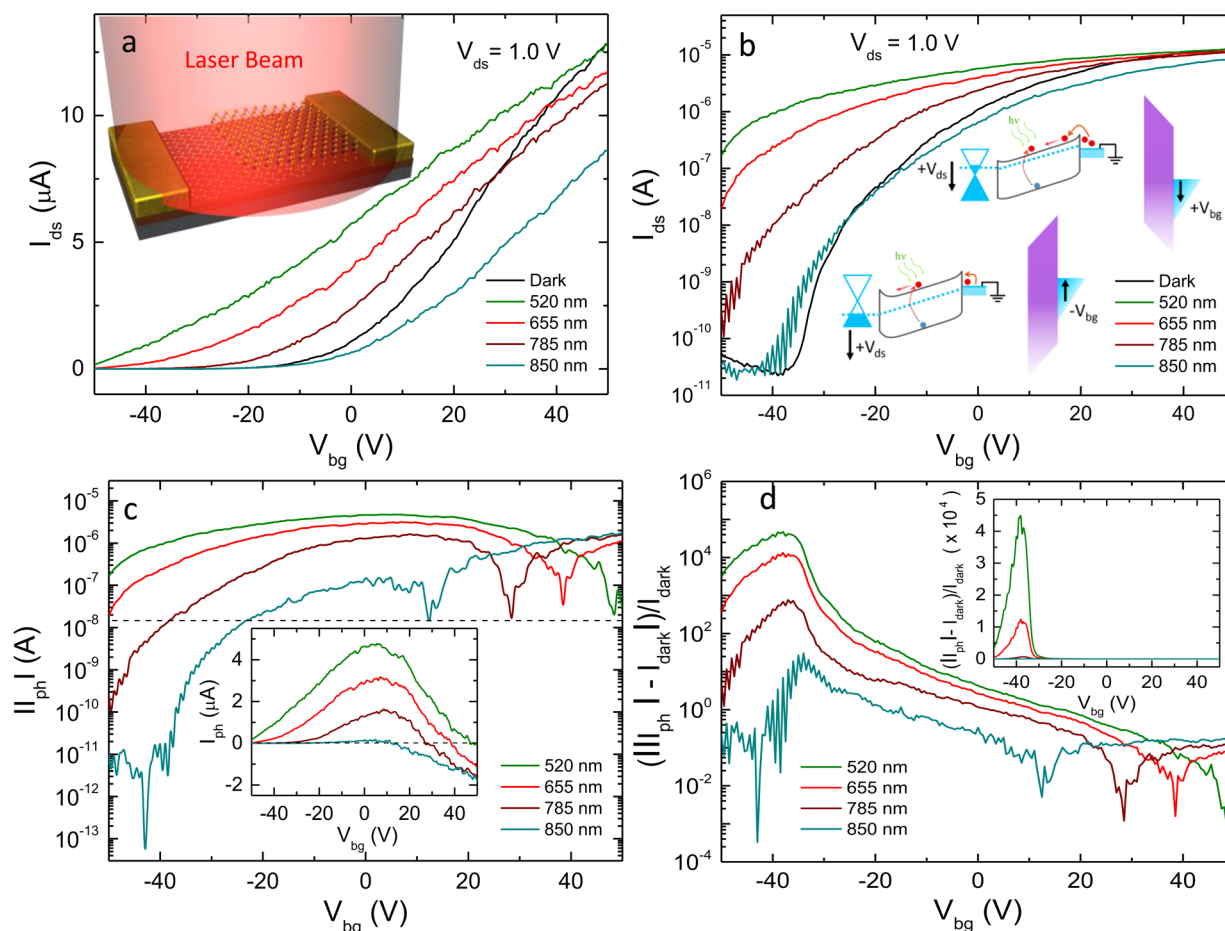


**Figure 5.** (a) Transfer characteristics on linear and (b) semilog scale in dark and under laser illumination where the inset in (a) shows a schematic of the illuminated device while in (b) shows band diagrams for illumination at far negative and positive gate voltages. (c) Variation of the photocurrent with back-gate voltage on semilog scale with the inset plotting the curves on linear scale. (d) Ratio of relative variation in photocurrent with back-gate voltage with the inset showing the plot on semilog scale for 520, 655, 785, and 850 nm wavelength light.

region becomes electron-doped (n-type) while the non-overlapped region are still p-type, resulting in pnp region. However, with increase of positive back-gate voltage, the nonoverlapped regions reaches the neutral point (+10 V) while the overlapped region becomes heavily electron doped, leading to the  $nn^+n$  configuration beyond the second Dirac point.

Finally, the optical characteristics of the asymmetrical graphene–MoS<sub>2</sub> device were measured using variable laser wavelength of 520 to 850 nm. Figure 4a shows the schematic of the fabricated device. In this device, a trilayer MoS<sub>2</sub> was exfoliated on a 300 nm SiO<sub>2</sub>/Si substrate and a single layer graphene was transferred thereon (for details, see Supporting Information, Section H). Figure 4b shows current versus drain voltage curves of the graphene–MoS<sub>2</sub> device at different back-gate voltages. The semilog curves plotted in Figure 4c illustrate that the linear curves, as seen in Figure 4b, appear only at high positive back-gate voltage and the typical rectified curves are observed for lower positive or negative gate voltages. These small variations in the device behavior can be due to various factors including variations in contact area, intrinsic doping level in both MoS<sub>2</sub> and graphene, and unintentional doping due to substrate. Figure 4d shows the transfer characteristics for drain voltage varying from 5.0 mV to 5.0 V with the on/off ratio, threshold voltage, and mobility of  $\sim 10^6$ ,  $-5$  V, and  $30 \text{ cm}^2(\text{V}\cdot\text{s})^{-1}$ , respectively, at room temperature. Figure 5a,b plots the transfer curves in response to the laser beam of different

wavelengths on linear and semilog scales, respectively. The global illumination of the device (as shown in the inset of Figure 5a) with the laser of 520, 655, and 785 nm has a minor effect on the on-current, whereas in the off-region the device turned on with a large current along with a prominent shift in the threshold voltage, which decreases gradually from 520 to 785 nm. However, in contrast to the other wavelengths, 850 nm laser shows a negative impact on the on-current, along with almost no shift in off-current and threshold voltage.

This dependence of photoresponse on back-gate voltage is illustrated in the inset of Figure 5b, which shows schematic band diagrams for negative and positive gate voltages, that is, in the off and on state, respectively. In the negative gate voltage regime, electrons are depleted in the MoS<sub>2</sub> channel, so the current is dominated by the photogenerated carriers, whereas in positive bias regime, the photogenerated current becomes comparatively negligible to the thermionic field current across the barrier. This can be seen clearly from the photocurrent ( $I_{ph}$ , defined as the difference between the illuminated current and dark current,  $I_{ph} = I_{\text{illuminated}} - I_{\text{dark}}$ ) plots in Figure 5c,d, where the photocurrent shows a clear back-gate voltage dependence. In general, the photocurrent decreases as the wavelength increases from 520 to 850 nm.<sup>1,34</sup> It can also be seen from Figure 5c,d that for all wavelengths, the photocurrent peaks at a certain gate voltage and decreases thereafter. These photocurrent peaks, as observed in the inset of Figure 5c, most likely

originate from the barrier height dependent contributions of the MoS<sub>2</sub>–metal and –graphene junction to the photocurrent,<sup>35–40</sup> as the effective barrier height of the junctions, especially graphene–MoS<sub>2</sub>, varies with the back-gate voltage.<sup>14,41</sup> On the other hand, the relative photocurrent peaks observed on the semilog and linear plots of the main and inset of Figure 5d, respectively, illustrate the relative contribution of the thermionic field current. Similarly, the negative photocurrent, which is observed after a certain back-gate voltage for all the wavelengths in Figure 5c,d with the crossover point decreasing from 48.3 to 38.5 V to 28.5 to 12.4 V for 520, 655, 785, and 850 nm, respectively, either owns its origin to the junction effect or related to the high carrier density and traps/impurity states response and their nonlocal hot-carrier behavior.<sup>42</sup> It may be noted that a slight variation in the dark current was observed after illumination, especially for 785 and 850 nm wavelength, where the device took very long time (few hours) to recover; however, for 520 and 655 nm, recovery was relatively quick (few minutes). This delay in the recovery can be due to the persistent photoconductance (PPC) phenomenon, which has been observed in other studies as well.<sup>2,3</sup> This phenomenon is related to the complex decay-time behavior of exciton relaxation and recombination through traps and impurities states. In addition to PPC phenomenon, impurities and dangling bonds at the layer and SiO<sub>2</sub> interface along with adsorbent molecules in the ambient environment also lead to hysteresis behavior in the transfer characteristics (for details, see Supporting Information, Section H).

Quantitatively, the optical response has been characterized by the responsivity ( $R = I_{ph}/P_{in}$ ) defined as the ratio of the photocurrent to the incident optical power, where  $P_{in}$  is the incident power.<sup>3,34,43</sup> The maximum values of  $R$  obtained for 520 nm light for an incident optical power density of 14 mW cm<sup>-2</sup> is  $\sim 2.06 \times 10^3$  AW<sup>-1</sup>, which is significantly higher than the published results.<sup>3,43</sup> Further, for more suitable comparison the specific detectivity  $D^*$ , which is a more useful metric for direct comparison between devices of different geometry, is also calculated using the following expression,  $D^* = A^{1/2}/NEP$  where  $A$  is the photodetector area and NEP is the noise equivalent power,  $NEP \approx (2qI_{dark})^{1/2}/R$  by considering a dominating shot noise in the dark current. For  $V_{ds} = 1.0$  V,  $V_{bg} = 4.0$  V, and  $D^* \approx 1.5 \times 10^{10}$  Jones, which is in good agreement with the other published results based on MoS<sub>2</sub> photodetector.<sup>34,44</sup>

In summary, graphene–MoS<sub>2</sub> heterostructure devices were fabricated, and their electrical and optical properties were measured. In addition to exhibiting rectifying characteristics due to asymmetric barrier, the devices displayed tunable behavior, controlled by the external gate. The cross-connected MoS<sub>2</sub> with metal contacts exhibited typical FET behavior with a high on–off ratio, the transfer characteristics of the cross-connected graphene with MoS<sub>2</sub> in between exhibited a double Dirac point, which is interpreted in terms of charge transfer from MoS<sub>2</sub> to graphene. For optical characterization, optical response to various wavelengths was measured, and 520 nm wavelength light resulted in the maximum photocurrent behavior. Besides, highlighting the fundamental understanding of layered heterojunction behavior and the present study can be useful in potential application of these structures in optics and electronic devices.

## ■ ASSOCIATED CONTENT

### ■ Supporting Information

Device fabrication method, Raman spectra, electrical characteristics of other graphene and MoS<sub>2</sub> device. Calculation of Fermi level shift and ideality factor. Application of tunable diode as a alternating current rectifier for sine and square wave. Photocurrent for laser 520, 655, 785, and 850 nm wavelength with hysteresis. The Supporting Information is available free of charge on the ACS Publications website at DOI: 10.1021/acs.nanolett.5b01030.

## ■ AUTHOR INFORMATION

### Corresponding Author

\*E-mail: ghkim@skku.edu.

### Notes

The authors declare no competing financial interest. S.R. and I.L. are co-first authors.

## ■ ACKNOWLEDGMENTS

This research was supported by Basic Science Research Program through the National Research Foundation of Korea (NRF) funded by the Ministry of Education, Science, and Technology (2013R1A2A2A01069023). G.H.L. acknowledges support from the Basic Science Research Program (NRF-2014R1A1A1004632) through the National Research Foundation (NRF) funded by the Korean government Ministry of Science, ICT, and Future and in part by the Yonsei University Future-leading Research Initiative of 2014.

## ■ REFERENCES

- (1) Yu, W. J.; Liu, Y.; Zhou, H.; Yin, A.; Li, Z.; Huang, Y.; Duan, X. *Nat. Nanotechnol.* **2013**, *8*, 952–958.
- (2) Roy, K.; Padmanabhan, M.; Goswami, S.; Sai, T. P.; Ramalingam, G.; Raghavan, S.; Ghosh, A. *Nat. Nanotechnol.* **2013**, *8*, 826–830.
- (3) Lopez-Sanchez, O.; Lembke, D.; Kayci, M.; Radenovic, A.; Kis, A. *Nat. Nanotechnol.* **2013**, *8*, 497–501.
- (4) Yu, W. J.; Li, Z.; Zhou, H.; Chen, Y.; Wang, Y.; Huang, Y.; Duan, X. *Nat. Mater.* **2013**, *12*, 246–252.
- (5) Yang, H.; Heo, J.; Park, S.; Song, H. J.; Seo, D. H.; Byun, K.-E.; Kim, P.; Yoo, I.; Chung, H.-J.; Kim, K. *Science* **2012**, *336*, 1140–1143.
- (6) Shih, C.; Wang, Q. H.; Son, Y.; Jin, Z.; Blankshtein, D.; Strano, M. S. *ACS Nano* **2014**, *8*, 5790–5798.
- (7) Kwak, J. Y.; Hwang, J.; Calderon, B.; Alsallman, H.; Munoz, N.; Schutter, B.; Spencer, M. G. *Nano Lett.* **2014**, *14*, 4511–4516.
- (8) Laroche, D.; Gervais, G.; Lilly, M. P.; Reno, J. L. *Nat. Nanotechnol.* **2011**, *6*, 793–797.
- (9) Ponomarenko, L. A.; Gorbachev, R. V.; Yu, G. L.; Elias, D. C.; Jalil, R.; Patel, A. A.; Mishchenko, A.; Mayorov, A. S.; Woods, C. R.; Wallbank, J. R.; et al. *Nature* **2013**, *497*, 594–597.
- (10) Baugher, B. W. H.; Churchill, H. O. H.; Yang, Y.; Jarillo-herrero, P. *Nat. Nanotechnol.* **2014**, *9*, 262–267.
- (11) Georgiou, T.; Jalil, R.; Belle, B. D.; Britnell, L.; Gorbachev, R. V.; Morozov, S. V.; Kim, Y.-J.; Gholinia, A.; Haigh, S. J.; Makarovskiy, O.; Eaves, L.; Ponomarenko, L. A.; Geim, A. K.; Novoselov, K. S.; Mishchenko, A. *Nat. Nanotechnol.* **2013**, *8*, 100–103.
- (12) Britnell, L.; Gorbachev, R. V.; Geim, A. K.; Ponomarenko, L. A.; Mishchenko, A.; Greenaway, M. T.; Fromhold, T. M.; Novoselov, K. S.; Eaves, L. *Nat. Commun.* **2013**, *4*, 1794.
- (13) Ross, J. S.; Klement, P.; Jones, A. M.; Ghimire, N. J.; Yan, J.; Mandrus, D. G.; Taniguchi, T.; Watanabe, K.; Kitamura, K.; Yao, W.; Cobden, D. H.; Xu, X. *Nat. Nanotechnol.* **2014**, *9*, 268–272.
- (14) Lin, Y.-F.; Li, W.; Li, S.-L.; Xu, Y.; Aparecido-Ferreira, A.; Komatsu, K.; Sun, H.; Nakaharai, S.; Tsukagoshi, K. *Nanoscale* **2014**, *6*, 795–799.
- (15) Sinha, D.; Lee, J. U. *Nano Lett.* **2014**, *14*, 4660–4664.

- (16) Das, S.; Gulotty, R.; Sumant, A. V.; Roelofs, A. *Nano Lett.* **2014**, *14*, 2861–2866.
- (17) Lee, Y. T.; Choi, K.; Lee, H. S.; Min, S.-W.; Jeon, P. J.; Hwang, D. K.; Choi, H. J.; Im, S. *Small* **2014**, *10*, 2356–2361.
- (18) Tian, H.; Tan, Z.; Wu, C.; Wang, X.; Mohammad, M. A.; Xie, D.; Yang, Y.; Wang, J.; Li, L.-J.; Xu, J.; Ren, T.-L. *Sci. Rep.* **2014**, *4*, 1–9.
- (19) Zhang, W.; Chu, C.-P.; Huang, J.-K.; Chen, C.-H.; Tsai, M.-L.; Chang, Y.-H.; Liang, C.-T.; Chen, Y.-Z.; Chueh, Y.-L.; He, J.-H.; Chou, M.-Y.; Li, L.-J. *Sci. Rep.* **2014**, *4*, 1–8.
- (20) Lu, C.-P.; Li, G.; Watanabe, K.; Taniguchi, T.; Andrei, E. Y. *Phys. Rev. Lett.* **2014**, *113*, 156804–5.
- (21) Makarova, M.; Okawa, Y.; Aono, M. *J. Phys. Chem. C* **2012**, *116*, 22411–22416.
- (22) Yu, Z.; Pan, Y.; Shen, Y.; Wang, Z.; Ong, Z.-Y.; Xu, T.; Xin, R.; Pan, L.; Wang, B.; Sun, L.; Wang, J.; Zhang, G.; Zhang, Y. W.; Shi, Y.; Wang, X. *Nat. Commun.* **2014**, *5*, 1–5.
- (23) Hui, Y. Y.; Liu, X.; Jie, W.; Chan, N. Y.; Hao, J.; Hsu, Y.-T.; Li, L.-J.; Guo, W.; Lau, S. P. *ACS Nano* **2013**, *7*, 7126–7131.
- (24) Ganatra, R.; Zhang, Q. *ACS Nano* **2014**, *8*, 4074–4099.
- (25) Nistor, R. A.; Kuroda, M. A.; Maarouf, A. A.; Martyna, G. J. *Phys. Rev. B* **2012**, *86*, 041409–5.
- (26) Yu, L.; Lee, Y.-H.; Ling, X.; Santos, E. J. G.; Shin, Y. C.; Lin, Y.; Dubey, M.; Kaxiras, E.; Kong, J.; Wang, H.; Palacios, T. *Nano Lett.* **2014**, *14*, 3055–3063.
- (27) Bao, W.; Cai, X.; Kim, D.; Sridhara, K.; Fuhrer, M. S. *Appl. Phys. Lett.* **2013**, *102*, 042104.
- (28) Chu, L.; Schmidt, H.; Pu, J.; Wang, S.; Ozyilmaz, B.; Takenobu, T.; Eda, G. *Sci. Rep.* **2014**, *4*, 1–6.
- (29) Barraza-Lopez, S.; Vanević, M.; Kindermann, M.; Chou, M. Y. *Phys. Rev. Lett.* **2010**, *104*, 076807–4.
- (30) Di Bartolomeo, A.; Santandrea, S.; Giubileo, F.; Romeo, F.; Petrosino, M.; Citro, R.; Barbara, P.; Lupina, G.; Schroeder, T.; Rubino, A. *Diam. Relat. Mater.* **2013**, *38*, 19–23.
- (31) Nam, Y.; Lindvall, N.; Sun, J.; Park, Y. W.; Yurgens, A. *Carbon* **2012**, *50*, 1987–1992.
- (32) Di Bartolomeo, A.; Giubileo, F.; Santandrea, S.; Romeo, F.; Citro, R.; Schroeder, T.; Lupina, G. *Nanotechnology* **2011**, *22*, 275702.
- (33) Özyilmaz, B.; Jarillo-Herrero, P.; Efetov, D.; Abanin, D.; Levitov, L.; Kim, P. *Phys. Rev. Lett.* **2007**, *99*, 166804–4.
- (34) Choi, W.; Cho, M. Y.; Konar, A.; Lee, J. H.; Cha, G.; Hong, S. C.; Kim, S.; Kim, J.; Jena, D.; Joo, J.; Kim, S. *Adv. Mater.* **2012**, *24*, 5832–5836.
- (35) Mueller, T.; Xia, F.; Avouris, P. *Nat. Photonics* **2010**, *4*, 297–301.
- (36) Herring, P. K.; Hsu, A. L.; Gabor, N. M.; Shin, Y. C.; Kong, J.; Palacios, T.; Jarillo-Herrero, P. *Nano Lett.* **2014**, *14*, 901–907.
- (37) Gabor, N. M.; Zhong, Z.; Bosnick, K.; Park, J.; McEuen, P. L. *Science* **2009**, *325*, 1367–1371.
- (38) Zhang, Q.; Jie, J.; Diao, S.; Shao, Z.; Zhang, Q. *ACS Nano* **2015**, *9*, 1561–1570.
- (39) Fontana, M.; Deppe, T.; Boyd, A. K.; Rinzan, M.; Liu, A. Y.; Paranjape, M.; Barbara, P. *Sci. Rep.* **2013**, *3*, 1634–5.
- (40) Li, H.-M.; Lee, D.-Y.; Choi, M. S.; Qu, D.; Liu, X.; Ra, C.-H.; Yoo, W. J. *Sci. Rep.* **2014**, *4*, 1–7.
- (41) Das, S.; Chen, H.; Penumatcha, A. V.; Appenzeller, J. *Nano Lett.* **2013**, *13*, 100–105.
- (42) Gabor, N. M.; Song, J. C. W.; Ma, Q.; Nair, N. L.; Taychatanapat, T.; Watanabe, K.; Taniguchi, T.; Levitov, L. S.; Jarillo-Herrero, P. *Science* **2011**, *334*, 648–652.
- (43) Zhang, W.; Huang, J.-K.; Chen, C.-H.; Chang, Y.-H.; Cheng, Y.-J.; Li, L.-J. *Adv. Mater.* **2013**, *25*, 3456–3461.
- (44) Tsai, D.-S.; Liu, K.-K.; Lien, D.-H.; Tsai, M.-L.; Kang, C.-F.; Lin, C.-A.; Li, L.-J.; He, J.-H. *ACS Nano* **2013**, *7*, 3905–3911.